

## PLASMA DYNAMICS ABOVE SOLAR FLARE SOFT X-RAY LOOP TOPS

G. A. DOSCHEK<sup>1</sup>, D. E. MCKENZIE<sup>2</sup>, AND H. P. WARREN<sup>1</sup>

<sup>1</sup> Space Science Division, Naval Research Laboratory, Washington, DC 20375, USA

<sup>2</sup> Montana State University, Bozeman, MT 59717, USA

Received 2013 December 4; accepted 2014 April 14; published 2014 May 19

### ABSTRACT

We measure non-thermal motions in flare loop tops and above the loop tops using profiles of highly ionized spectral lines of Fe XXIV and Fe XXIII formed at multimillion-degree temperatures. Non-thermal motions that may be due to turbulence or multiple flow regions along the line of sight are extracted from the line profiles. The non-thermal motions are measured for four flares seen at or close to the solar limb. The profile data are obtained using the Extreme-ultraviolet Imaging Spectrometer on the *Hinode* spacecraft. The multimillion-degree non-thermal motions are between 20 and 60 km s<sup>-1</sup> and appear to increase with height above the loop tops. Motions determined from coronal lines (i.e., lines formed at about 1.5 MK) tend to be smaller. The multimillion-degree temperatures in the loop tops and above range from about 11 MK to 15 MK and also tend to increase with height above the bright X-ray-emitting loop tops. The non-thermal motions measured along the line of sight, as well as their apparent increase with height, are supported by *Solar Dynamics Observatory* Atmospheric Imaging Assembly measurements of turbulent velocities in the plane of the sky.

**Key words:** Sun: activity – Sun: flares – Sun: UV radiation

**Online-only material:** color figures

### 1. INTRODUCTION

The most tantalizing aspect of solar flares is the so-called reconnection region, situated in the current sheet above the soft X-ray-emitting flare loops. This region is the least well observed area of flares and probably the most difficult to understand theoretically, but it is also the most important flare region, as it is believed that this is where flares and some coronal mass ejections (CMEs) are initiated. The current belief of many is that the reconnection region initiates non-thermal particle acceleration and plasma heating, producing energetic particles and conduction fronts that propagate downward into the chromosphere, causing chromospheric evaporation. The actual particle acceleration and heating may occur outside of and adjacent to the reconnection region. Also, at least for long-duration flares, reconnection may be centrally important for the production of an outward-propagating CME. The reconnection region is the heart of the so-called standard flare model.

In the standard flare model, reconnection results in a rearrangement of magnetic field that produces outward-propagating magnetic fields that sometimes contain CMEs and closed flux tubes below the reconnection region that fill up with evaporated multimillion-degree plasma producing the X-ray and EUV emission observed in solar flares. This plasma cools, producing lower temperature emission. Many details of this model have not been investigated quantitatively due to the lack of sophisticated instrumentation necessary, i.e., telescopes and spectrometers with high spatial, spectral, and temporal resolution, and a dynamical range that can accommodate the huge intensity variations of a flare in the EUV and X-ray ranges. In particular, physical conditions in the reconnection region are not well known.

Theoretically, magnetic reconnection is extremely difficult to model (e.g., Yamada et al. 2010; Zweibel & Yamada 2009). Models that have been made reveal the possibility of magnetic islands, accelerated particles, shocks, flows, and turbulence (e.g., Drake et al. 2006; Hamilton & Petrosian 1992; Liu et al. 2008). Measurements of physical parameters such as

temperature, density, turbulence, and flows are needed for every aspect of the standard flare model, from the reconnection region to the footpoints of loops in the chromosphere.

Observations of flares before the era of *Hinode*, *STEREO*, and the *Solar Dynamics Observatory* (*SDO*) have provided important information on the structure of flares. Many of these observations come from instruments on the Japanese *Yohkoh* spacecraft. The temperature and density structure in the vicinity of the soft X-ray-emitting loop tops was measured by Tsuneta (1996) using images from the Soft X-ray Telescope (SXT) on *Yohkoh*. Tsuneta (1996) was also able to deduce reconnection inflow and outflow speeds from the flare morphology, temperature and density measurements, and theory. Reconnection outflows were also inferred from SXT images by McKenzie (2000), while signatures of reconnection inflows were detected in images from EIT on the *Solar and Heliospheric Observatory* (*SOHO*) by Yokoyama et al. (2001). The maximum thermal temperature of flares as a function of *GOES* X-ray class was determined using Bragg crystal spectrometers (BCS) on *Yohkoh* (e.g., Feldman et al. 1995, 1996), which were sensitive to higher temperatures than SXT. However, these spectrometers had no spatial resolution, and so the locations of temperatures in the flares could not be determined.

Spatially resolved direct measurements of flows and/or non-thermal motions, i.e., either turbulence or unresolved flows, are far fewer than indirect measurements based on images and theory. Spatially unresolved measurements of evaporation speeds and non-thermal motions in flares are abundant, mostly from Bragg spectrometers on the Japanese *Hinotori* spacecraft, the U.S. Department of Defense *P78-1* mission, the NASA *Solar Maximum Mission* (*SMM*), and *Yohkoh*. An exception is Bragg crystal measurements made by Mariska & McTiernan (1999) on *Yohkoh* limb flares that were partially occulted by the limb. There are also spatially resolved observations available from the NASA 8th *Orbiting Solar Observatory* and from the Coronal Diagnostics Spectrometer (CDS) and Solar Ultraviolet Measurements of Emitted Radiation (SUMER) spectrometers

on *SOHO* (e.g., Czaykowska et al. 1999; Wang et al. 2007; Innes et al. 2003). With CDS, Czaykowska et al. (1999) observed chromospheric evaporation in the late gradual phase of a flare and concluded that magnetic reconnection continues to occur through the late phase. Wang et al. (2007) observed high-speed jets, which they interpret as direct evidence of high-speed magnetic reconnection outflows in the current sheet in the corona. Innes et al. (2003) observed dark downward-moving structures against the bright EUV arcade of a limb flare using both *Transition Region and Coronal Explorer* and SUMER data. They obtained spatially resolved Doppler speeds and emission measures over a temperature range from  $2 \times 10^4$  K to  $10^7$  K.

Many more flare observations are now being made since the launch of the *Hinode* spacecraft (Kosugi et al. 2007) that contains the Extreme-ultraviolet Imaging Spectrometer (EIS) (e.g., Culhane et al. 2007) and the Atmospheric Imaging Assembly (AIA) EUV imagers on *SDO* (Lemen et al. 2012). EIS has an angular resolution of about 2" and a spectral resolution sufficient to measure Doppler and non-thermal motions for EUV spectral lines that cover a temperature range from about 0.1 MK up to about 15 MK. Interpretation of the EIS data is augmented considerably by imaging data from the X-Ray Telescope on *Hinode* (Golub et al. 2007) and images from the AIA telescopes on *SDO*. EIS measurements of flows and non-thermal motions at specific locations in flares have been made by a number of authors (e.g., Hara et al. 2008; Harra et al. 2009; Milligan & Dennis 2009; Milligan 2011; Hara et al. 2011; Young et al. 2013; Doschek et al. 2013; Imada et al. 2013). These observations are enabling tests of aspects of the standard model such as chromospheric evaporation. In the case of evaporation, observations are available at footpoint regions from lines formed over a large range of temperature, i.e., from about 0.1 MK up to about 15 MK.

Spectroscopic observations above flare soft X-ray loop tops, in the dark areas between the loop tops and the reconnection region, are still not abundant. It is necessary to observe flares near or at the limb such that the line-of-sight does not involve the soft X-ray-emitting loops (e.g., Hara et al. 2008). In this paper we present EIS results of non-thermal motions at multimillion-degree temperatures in the areas immediately above the soft X-ray-emitting loops for four flares that occurred near or at the limb. These are motions in excess of those expected from thermal Doppler effects. They are either turbulence or unresolved multiple flows along the line of sight. Plane-of-sky velocities found via local correlation tracking (LCT) applied to AIA images of the same region assist in investigating the nature of these motions.

The times of the flare observations we have chosen are mostly after the impulsive phase and peak X-ray flux. During the impulsive phase, heating produced near the reconnection region as a result of the reconnection process produces high-energy particles and conduction fronts that propagate along field lines to the chromosphere. The chromosphere is heated and evaporates (ablates) multimillion-degree plasma into closed loops that are produced by the reconnection. This produces intense X-ray emission as a result of the high-temperature plasma and increasing density in the loops. The speed of the evaporating plasma can be several hundred kilometers per second, which can produce striking asymmetric spectral line profiles (mostly a blueshifted component but possibly also redshifted components) during the early impulsive phase (e.g., Reeves et al. 2007; Warren & Doschek 2005). This can be further complicated by surges, which can produce both blueshifted and redshifted

components. The actual shapes of line profiles have a critical dependence on the orientation of the flare loops with respect to the observer. As the loops fill up, they increase in density and the evaporation speeds decrease, resulting in a decrease of the evaporation signatures in line profiles. During the impulsive phase, the evaporating plasma and surges make it difficult to disentangle these dynamical effects from a random non-thermal motion. However, the observations we analyze are made after the strong bulk flows have lessened and/or are absent. The line profiles are highly symmetric and well fit by single Gaussian profiles.

In previous work using X-ray spectra described in Section 4, it was found that non-thermal motions are independent of flare position, indicating symmetry in their spectral broadening. As mentioned, the high spectral resolution BCS flown in the late 1970s and 1980s observed the entire flare (including footpoints with evaporating plasma). The question arose as to how much of the observed line widths is due to true non-thermal motions, and how much is due to evaporating plasma or unresolved flows in flux tubes? This question was debated during the *Solar Maximum Mission* Workshop (Doschek et al. 1986). The answer is that the non-thermal motion measurements are reliable and separate from the flows. The question was answered by Antonucci et al. (1986), who showed from *SMM* spectra that the non-thermal motions are independent of solar longitude while the evaporating effects on line profiles are not. That is, most of the flows are biased in the solar radial direction and should therefore vanish at the limb. This was true for the evaporating spectral line signatures, but not true for the non-thermal motions. Instead, Antonucci et al. (1986) argue that the non-thermal motions are due to flows generated by many reconnection sites in the flare leading to turbulent motions and are not due to evaporating plasma. This picture is consistent with current observations.

Although the observations are made after flare maximum, the post-flare loops are nevertheless strong and continually evolving. Furthermore, high temperatures on the order of 10 MK persist at the loop tops. Analysis of emission measure distributions in flares indicates continual heating well beyond the impulsive phase (e.g., Warren et al. 2013). We feel that this heating is due to continual magnetic reconnection, as concluded earlier by Czaykowska et al. (1999), but we cannot demonstrate that this must be the case. Perhaps most interesting regarding the longevity of magnetic reconnection is provided by the suprarcade downflows discussed by many authors (e.g., McKenzie & Hudson 1999; McKenzie 2000; Sheeley et al. 2004; McKenzie & Savage 2009; Warren et al. 2011).

## 2. SPECTRA AND DATA REDUCTION

The EIS imaging spectrometer observes two narrow wavelength bands between about 170–213 Å and 250–290 Å. A telescope feeds a spectrometer through one of four possible slit/slot apertures oriented in the north–south direction. For the flare observations to be described, a 1" or 2" slit was used. There are a number of flare studies, i.e., software programs that select spectral lines for observations, the mode of observation, exposure times, etc. The flares we observe were obtained with two studies: HH\_Flare\_raster\_v3 and FlareRespTest1. These are studies in which the slit is stepped in increments across the flare region repetitively. Some details of the rasters are given in Tables 1 and 2.

The study in Table 2 contains more lines and takes smaller raster steps than the study in Table 1. However, it can only be

**Table 1**  
HH\_Flare\_raster\_v3 Flare Study

Slit: 2"
Number of lines: 11
Number of slit positions: 29 (X-range: 174")
Y-range: 152"
Raster step size: 6"
Exposure time per spectrum: 9 s

**Table 2**  
FlareRespTest1 Flare Study

Slit: 2"
Number of lines: 14
Number of spectra: 79 (X-range: 237")
Y-range: 304"
Raster step size: 3"
Exposure time per spectrum: 5 s

run in response to a flare trigger. If run continuously, it would quickly consume all the EIS telemetry allocation. The study in Table 1 can be run more continuously than the study in Table 2, but it contains fewer spectral lines and has lower spatial resolution. The EIS flare spectra are corrected using standard EIS software for dark current, the CCD pedestal, temperature variations caused by orbiting the Earth, slit tilt, and warm pixels.

Non-thermal motions are derived from the widths of the spectral lines, which in the absence of chromospheric evaporation or downflow signatures appear close to Gaussian profiles. We have fit data for multimillion-degree flare lines of Fe xxiv and Fe xxiii and some coronal lines ( $\sim 1$  MK) with Gaussian fits using the IDL GAUSSFIT routine. The FWHM of a spectral line is given by

$$\text{FWHM} = 1.665 \frac{\lambda}{c} \sqrt{\frac{2kT}{M} + V^2 + W_I^2}, \quad (1)$$

where  $\lambda$  is the wavelength (in Å in this paper),  $c$  is the speed of light,  $k$  is the Boltzmann constant,  $T$  is the electron temperature, and  $M$  is the ion mass. The line is broadened by three components that are all also assumed Gaussian with the same rest wavelengths. Lines are considerably broadened by the instrumental width,  $W_I$ . For the 2" slit this width varies across the CCD in the north-south direction. The instrumental width at each pixel location has been removed using EIS Software Note No. 7 prepared by Peter Young.

In addition to instrumental broadening, lines are broadened by thermal Doppler motions at the temperature  $T$  where they are formed and by the non-thermal motions  $V$ . For the multimillion-degree flare lines the electron temperature is calculated from the ratio of the Fe xxiii  $\lambda 263.76$  line to the Fe xxiv  $\lambda 255.10$  line. The calculation assumes that the sources above the flare loop tops are isothermal (there are an insufficient number of lines to attempt a detailed differential emission measure calculation) and ionization equilibrium is valid. Electron temperatures are derived from the line ratios using the atomic data in CHIANTI (e.g., Landi et al. 2013). For the coronal lines, the electron temperature of peak emitting efficiency of the lines has been assumed. The assumption is that these lines are produced in plasma cooling from multimillion-degree temperatures. Finally, the temperature in Equation (1) is really the ion temperature. We assume that at flare electron densities the ion and electron temperatures are equal. Removal of the instrumental and thermal

**Table 3**  
EIS Flares

Date	Start Time (UT)	Location	GOES Class	EIS Study
2012 Jan 27	17:37	N29 W91	X1.7	HH_Flare_raster_v3
2012 May 17	01:25	N13 W83	M5.1	HH_Flare_raster_v3
2013 May 15	01:25	N12 E64	X1.2	HH_Flare_raster_v3
2013 Jun 7	22:11	S31 W82	M5.9	FlareRespTest1 Flare Study

Doppler broadening yields the non-thermal velocities  $V$  using Equation (1).

### 3. THE FLARE OBSERVATIONS

EIS has observed four near limb flares (see Table 3) for which non-thermal motions can be derived that are not contaminated by the soft X-ray loops. These flares are complex and have specific structures of interest. First, we show pixel-by-pixel results for the 2012 May 17 flare, and then we give averages within boxes in different areas above the flare loop tops. The averages are more robust than pixel-by-pixel values, which suffer much more from statistical uncertainties. Errors are discussed at the end of this section.

#### 3.1. The 2012 May 17 Flare

The first EIS raster for the 2012 May event began at 02:28:18 UT, well after the peak of the event. At the beginning of the raster the flare was approximately an M1.8 flare. Figure 1 shows the GOES plot, an EIS raster image in a spectral line of Fe xiv at 264.78 Å, and an AIA 193 Å filter image made near 05 UT. Images in this filter earlier than about 5 UT are saturated. A comparison of the AIA image with the EIS image in a line not far in temperature from the lines in the AIA filter shows the spatial resolution obtained by EIS in a picket-fence raster where the slit is stepped in units larger than the slit width. Although not a high-resolution image such as obtained with the 1" slit stepping in increments of 1", the similarity of the filter image and EIS image is obvious. There is one clear loop arcade and a region farther north that is probably also an arcade. The southern region is brighter in the EIS image evidently because it was obtained at a much earlier time than the AIA image. The white lines in the EIS image define the area of the raster encompassed by the images and results in Figures 2–5.

Intensity images of the flare are shown in Figure 2 for several lines formed over a range of temperatures. The loop orientation is such that the regions above the loop tops are in the area approximately bounded by slit positions from about 70" to 120", i.e., the western (right) portion of the images. Note that in this area the peak intensity of the lines is a function of temperature of line formation, increasing toward the west (toward the reconnection region) as the temperature increases. For example, the peak intensity for the Fe xxiv line is at slit positions (X pixels) greater than 80" but the peak intensity of the coronal Fe xii line is at slit positions less than 80". This result is consistent with some standard flare model scenarios. In some standard flare model scenarios, plasma heating occurs in downward-contracting loops or in newly formed and heated high-lying static loops that subsequently cool. The highest lying contracting loops or newly formed static loops are hottest and then cool, leading to geometries where the temperature of the loops increases with loop size. These flare images and the results shown in the next three figures were obtained between 02:28 UT and 02:31 UT.

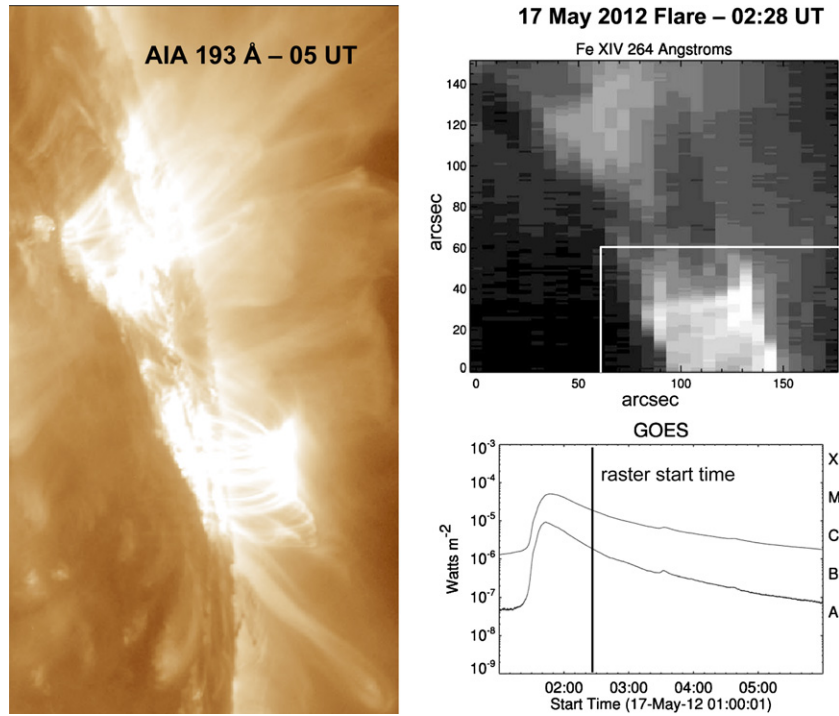


**Figure 1.** GOES X-ray light curves, an EIS image, and an AIA filter image of the 2012 May 17 limb flare. The white lines in the Fe XIV image define the area of the images, and results are shown in Figures 2, 3, 4, and 5.

(A color version of this figure is available in the online journal.)

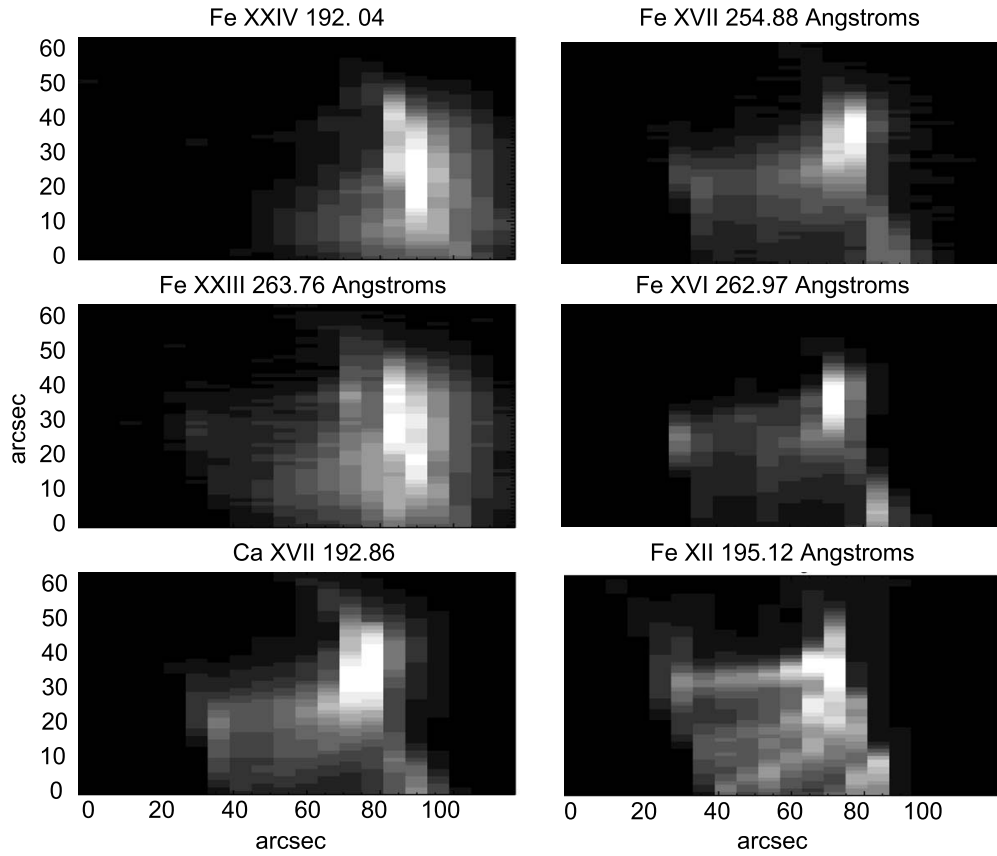


**Figure 2.** Intensity images of the May 17 flare for lines formed at different temperatures. The temperatures are Fe xxiv, 18 MK; Fe xxiii, 14 MK; Ca xvii, 6 MK; Fe xvii, 4 MK; Fe xvi, 2.8 MK; and Fe xii, 1.6 MK. The Ca xvii line is blended with a strong line of Fe xi, which explains its brightness at heights less than 80''.

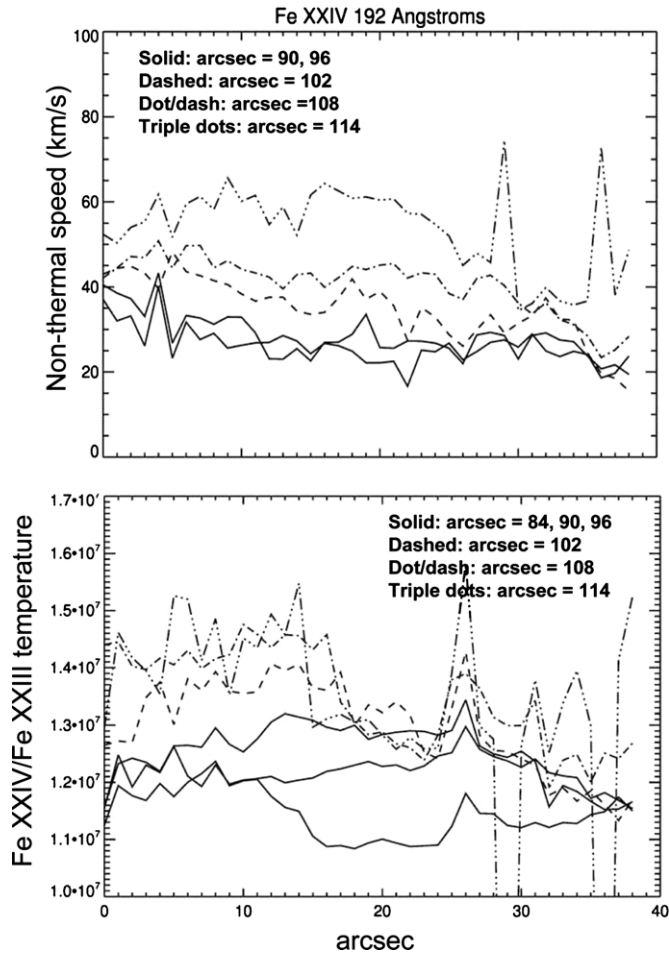


**Figure 3.** Top panel: non-thermal speeds at different heights above the soft X-ray-emitting loop tops. Bottom panel: the electron temperature for the same heights determined from the indicated line ratio assuming an isothermal plasma. The  $X$  axis is  $Y$  pixels in units of arcsec. See the text for a complete explanation of this figure.

The top panel of Figure 3 shows the Fe xxiv  $\lambda 192$  line non-thermal motions above the loop tops for five selected slit positions ( $X$ -axis pixels in Figure 2) as a function of the  $Y$ -axis pixels in Figure 2 (i.e., the  $X$  axis in Figure 3 is the  $Y$  axis of the Figure 2 image expressed in units of arcsec). From the orientation of the closed flare loops, the direction of the reconnection region in Figure 2 is roughly parallel to the Figure 2  $X$  axis. Therefore, as an example, the dot/dash curves in Figure 3 represent the slit position of  $108''$  along the  $X$  axis of Figure 2. In Figure 2 the position of the bright loop tops of Fe xxiv is at an  $X$ -axis position of about  $90''$ . Thus, the distance above the Fe xxiv loop tops toward the reconnection region of the dot/dash curve in Figure 3 is about  $108'' - 90'' = 18''$  or about  $1.3 \times 10^4$  km.

Figure 3 shows results for the first 40 Figure 2  $Y$  pixels that are directly above the loop tops. The Fe xxiv  $\lambda 192$  line is the strongest line with the best statistics. However, one must be careful close to the loop tops where at peak emission in M- and X-flares it will be saturated. Figure 3 shows that the non-thermal motions increase with height above the loop tops, and that the motions vary with position along the Figure 2  $Y$  axis. Variations along  $Y$  are expected since the  $Y$  axis runs almost parallel to the arcade and one expects variations for different regions along this axis. The height above the loop tops also increases with

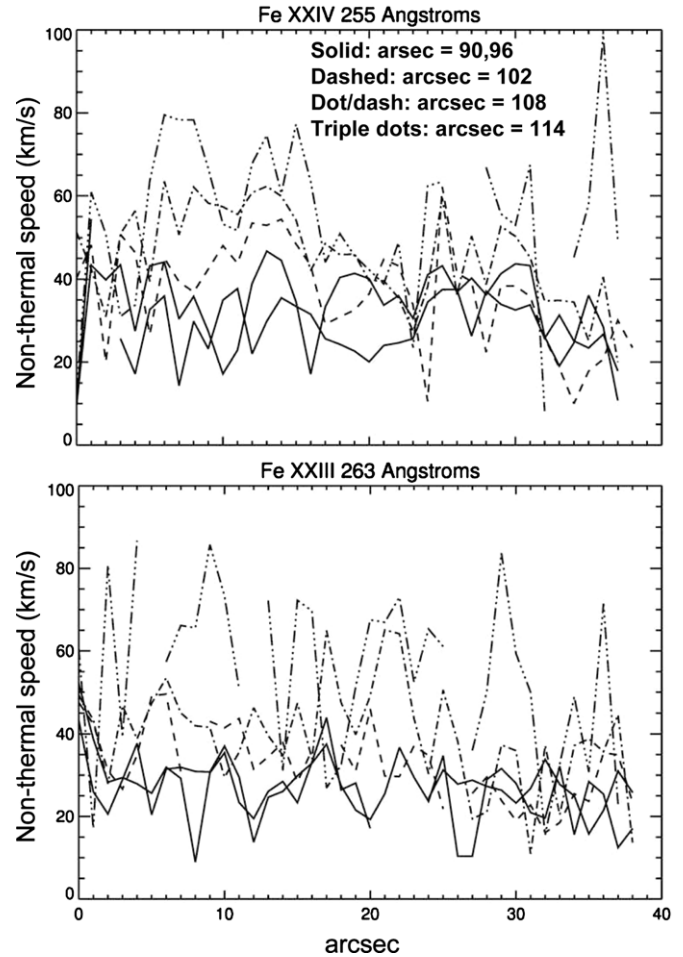


**Figure 4.** Non-thermal speeds at different heights above the soft X-ray-emitting loop tops for the lines indicated. The  $X$  axis is  $Y$  pixels in units of arcsecs.

increasing  $Y$ . The non-thermal motions are about  $20\text{--}30$  km s<sup>-1</sup> close to the loop tops and reach about  $60$  km s<sup>-1</sup> at the largest height visible in the Figure 2 raster.

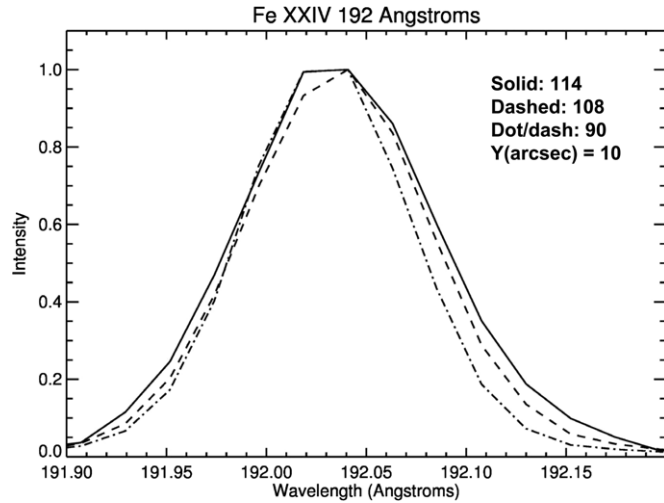
The bottom panel of Figure 3 shows the electron temperature in a plot similar to the top panel. The temperatures are also functions of the Figure 2  $Y$  pixels (in arcsecs) and vary between about 11 and 15 MK. These temperatures are typical for loop-top regions (e.g., Doschek & Feldman 1996; Mariska & Doschek 1997).

Figure 4 shows non-thermal speeds for the Fe xxiv  $\lambda 255$  line and the Fe xxiii  $\lambda 263$  line. The statistics are much worse for these lines than for the  $\lambda 192$  line, but the averages are in general agreement with the  $\lambda 192$  results.

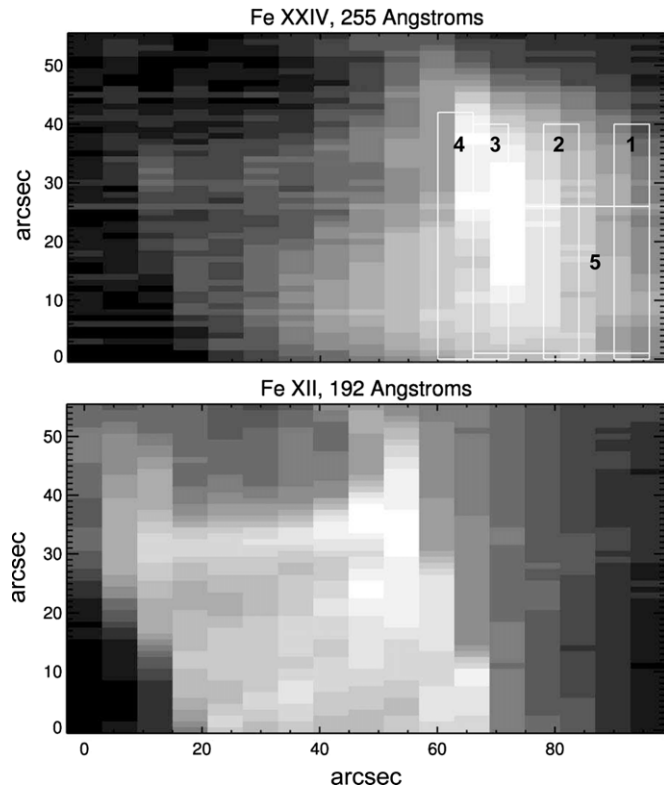
A similar analysis was performed for two later rasters, beginning at 02:33:39 UT and 02:39:00 UT. Similar non-thermal speeds, temperatures, and variations along the  $X$  and  $Y$  axes were obtained.

Figure 5 shows the Fe xxiv  $\lambda 192$  line profiles at three different slit positions for the same  $Y$  pixel ( $10''$ ) in the 02:28 UT raster as an example to demonstrate the magnitude of the variations in profile width. The profiles have been normalized to unity to facilitate the comparison.

Because the pixel-by-pixel results do not have good statistics except for the  $\lambda 192$  line, we have also computed results by summing data in boxes located at different heights above the loop tops. Figure 6 shows the boxes we have chosen superimposed on the 255 Å intensity image (top panel).



**Figure 5.** Line profiles of the strongest Fe xxiv line at three different slit positions for the  $Y$  pixel = 10''. The profiles are normalized to unity.



**Figure 6.** Intensity images in Fe xxiv and a line of Fe xii at 192.39 Å for the 2012 May 17 flare. The boxes indicate areas in which average non-thermal motions and temperatures were computed (see Table 4).

Box 5 is an average over a large portion of the region above the loop tops. For comparison to typical coronal temperature emission in the flare, the bottom panel shows the intensity image in a line of Fe xii at 192.39 Å.

The average non-thermal motions and temperatures in the five boxes in Figure 5 are given in Table 4. The results in Table 4 are consistent with the pixel-by-pixel results except that they do not show as well the highest non-thermal speeds that are obtained in the lines of Fe xxiv and Fe xxiii. This is because the boxes average over larger regions of  $X$  than the single-pixel results. Note that the Fe xii non-thermal motions are about the same everywhere. As mentioned, these speeds are computed

**Table 4**  
Average Non-thermal Motions and Fe xxiv Temperatures—2012 May 17 Flare

Box	Fe xxiv V (km s $^{-1}$ )	Fe xii V (km s $^{-1}$ )	Fe xxiv Temperature (MK)
1	49	28	13.6
2	34	33	12.7
3	28	35	11.8
4	28	41	11.4
5	40	36	13

**Table 5**  
Average Non-thermal Motions and Fe xxiv Temperatures—2013 June 7 Flare

Box	Fe xxiv V (km s $^{-1}$ )	Fe xii V (km s $^{-1}$ )	Fe xv V (km s $^{-1}$ )	Fe xxiv Temperature (MK)
1	57	16	28	13.2
2	40	16	27	13.4
3	32	16	28	13.1
4	22	13	31	12.1
5	38	19	31	13.0
6	25	15	31	12.4
7	40	18	31	12.9
8	44	15	28	13.2
9	62	20	32	13.2
10	38	16	33	11.5

assuming that Fe xii is emitted at its temperature of maximum emitting efficiency in ionization equilibrium.

The averages are computed for three high-temperature lines: Fe xxiv  $\lambda\lambda$  192 and 255, and the Fe xxiii line at 263 Å. In each box, some pixel data are not good. We also compute the number of pixels for which the data are good compared with the number of pixels in the box. If the number of good pixels is much less than the number of pixels in the box, then we consider the data not too reliable (further details are given below in Section 3.5). The problem might be due to poor counting statistics, warm pixels, or too much intensity, i.e., saturation. If there are a substantial number of good pixels, but some scatter in the value of the non-thermal motions in the Fe xxiv and Fe xxiii lines, we estimate from the three values a most probable value. We consider the results in Table 4 to be reliable.

### 3.2. The 2013 June 7 Flare

The June 7 event has the advantage of higher spatial resolution observations, as well as more spectral lines. Inspection of AIA data shows that the event is a large arcade. The AIA data are saturated near the time of the first EIS raster. However, inspection of the AIA data via JHelioviewer shows that the event is quite complex with different loops brightening and fading over time periods less than a minute.

The Fe xxiv emission in EIS images lies distinctly above the coronal emission such as Fe xii emission. It is also rather complex in morphology. Figure 7 shows some AIA 193 Å filter data, the EIS raster images in Fe xxiv and Fe xii, and the GOES data. We explore the average non-thermal motions in 10 different boxes mostly above the coronal X-ray loops. These boxes are shown in Figure 8.

The average non-thermal motions for Fe xxiv and Fe xii lines are shown in Table 5. For the June event, we also show the non-thermal speeds in the Fe xv line near 284 Å. Later, in Figure 14 we show that the Fe xxiv motions increase with height above the coronal loops visible in lines from ions such as Fe xii. These motions are about 30–60 km s $^{-1}$ . Close to the coronal loops

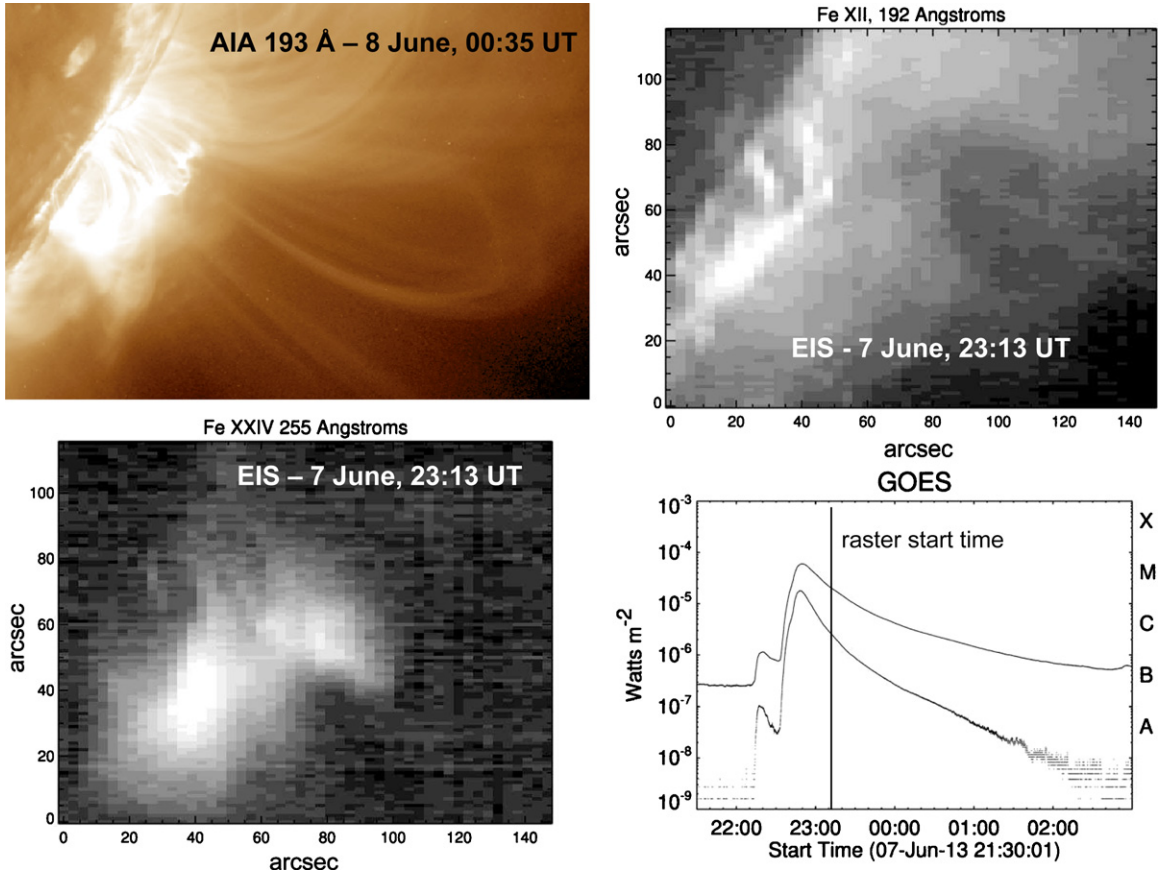


**Figure 7.** Top left: an AIA 193 Å image; top right and bottom left: EIS intensity images (log scale) in the indicated lines; bottom right: *GOES* data for the 2013 June 7 flare.

(A color version of this figure is available in the online journal.)

the motions are smaller,  $20\text{--}30 \text{ km s}^{-1}$ . The coronal motions in the Fe XII line are  $15\text{--}20 \text{ km s}^{-1}$ , and the motions in the somewhat hotter Fe XV line are about twice as large. The Fe XXIV temperatures are between 11 and 14 MK. Overall the results for the June 7 event agree with the results for the 2012 May 17 event.

A similar analysis was performed for a raster beginning at about 23:04 UT, 9 minutes earlier. The non-thermal motions in five similar boxes are close to the values found for the 23:13 UT raster.

The interpretation of Fe XII emission above the loop tops in which the emission is bright is unclear. In the standard flare model it is expected that these fainter higher regions are hot, and it is questionable whether or not Fe XII should be found there. But the emission could simply be due to the cooling of hotter loops. Or perhaps it is background emission from the surrounding corona. The fact that the non-thermal speeds are substantially less than the Fe XXIV speeds gives us confidence in the results in that both the Fe XII and Fe XXIV lines are very close in wavelength.

### 3.3. The 2013 May 15 Flare

The May 15 flare was observed from its beginning to well into the decay phase. The intensity of this flare is high; therefore, there is saturation of lines near the peak of the event, and care must be taken when computing line profiles. Figure 9 shows some AIA images well after the EIS raster we have chosen near 02:08 UT. EIS rasters before this raster have substantial

**Table 6**  
Average Non-thermal Motions and Fe XXIV Temperatures—2013 May 15 Flare

Box	Fe XXIV V (km s <sup>-1</sup> )	Fe XII V (km s <sup>-1</sup> )	Fe XXIV Temperature (MK)
1	32	25	13.2
2	50	20	14.4
3	60	18	14.7
4	35	21	13.6
5	42	15	13.3

saturation in the Fe XXIV line. Average non-thermal speeds and temperatures in five boxes (shown in Figure 10) are given in Table 6. We also examined the next raster near 02:13 UT and obtain similar results for boxes located in nearly the same location as in Figure 10. Inspection of Figure 10 and Table 6 again shows that non-thermal motions are largest above the bright closed flare loops.

### 3.4. The 2012 January 27 Flare

The January 27 flare is another large arcade limb event. Unfortunately, the EIS rasters do not cover a very large distance directly above the arcade, i.e., the tops of the hot loops are close to the north/northwestern border of the rasters. As the flare develops, the loops slowly drift even closer to the raster borders due to spacecraft drift. However, the first raster is quite interesting even though the Fe XXIV  $\lambda 192$  line is saturated because it was obtained near the peak soft X-ray emission.

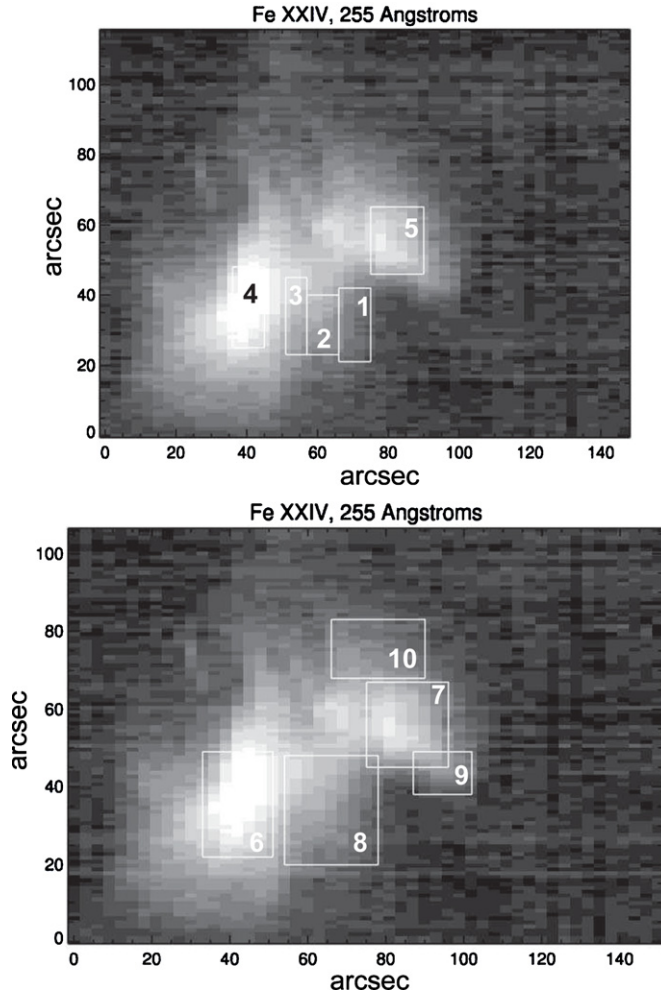


**Figure 8.** Intensity images in Fe xxiv for the 2013 June 7 flare. The boxes indicate areas in which average non-thermal motions and temperatures were computed (see Table 5).

**Table 7**

Average Non-thermal Motions and Fe xxiv Temperatures—2013 January 27 Flare

Box	Fe xxiv V (km s <sup>-1</sup> )	Fe xii V (km s <sup>-1</sup> )	Fe xxiv Temperature (MK)
1H	35	...	14.1
2H	39	...	13.1
3H	39	43	15.0
4H	39	19	14.2
5H	49	15	14.2

Figure 11 shows an AIA 193 Å filter image taken substantially after the EIS raster. At the time of the EIS raster, the AIA images are saturated. Nevertheless, the later image shows the orientation of the arcade. Figure 12 shows the boxes we have chosen for this event, and results are given in Table 7. The numbers in Table 7 are labeled H (for *Hinode*) to distinguish them from the numbered boxes in the *SDO/AIA* image described below. As mentioned, the Fe xxiv line is saturated, and the saturation also produces spurious results for the Fe xii line for two boxes because it is close in wavelength to the Fe xxiv line. In this event the non-thermal motions are somewhat less than in the other events.

Investigation of this flare is supplemented by analysis of EUV images from *SDO/AIA*. A long sequence of images

**Table 8**  
Median Non-thermal Motions at about 10 MK  
(Fe xxiv) for the 2013 January 27 Flare

Box	Fe xxi V (km s <sup>-1</sup> )
1	13
2	23
3	47
4	67

in the 131 Å channel was selected to cover the time range 19:00:21–23:20:58 UT; 645 images were selected with a cadence of one image per 24 s. The 131 Å channel primarily detects emission from Fe xxi in flares (O’Dwyer et al. 2010) and thus images plasmas with temperatures around 10–15 MK. The AIA images were pre-processed for contrast enhancement and then analyzed with LCT as described in McKenzie (2013). One contrast-enhanced snapshot is shown in Figure 13 to illustrate the region of interest.

The LCT analysis reveals significant velocity shears, with variations in local velocity on the order of 100–200 km s<sup>-1</sup> on length scales of just a few megameters. Calculation of the curl of the velocity field indicates vorticity that varies both temporally and spatially. Moreover, the contrast-enhanced AIA image sequence demonstrates that the plasma structures are perturbed and distorted on ever smaller length scales as the flow continues. To the degree that such an apparent cascade to smaller length scales, accompanied by spatially and temporally varying vorticity, is a hallmark of turbulence, we are led to conclude that the AIA images and the LCT analysis are strongly suggestive of turbulence in the plasma sheet above the arcade.

Over the 4.5 hr time span of the AIA images, the median plane-of-sky speed in the region is 40 km s<sup>-1</sup>. The turbulent motions in the plane of the sky, found by AIA, are thus of a similar magnitude as the speeds along the line of sight implied by the non-thermal broadening measured by EIS in nearly the same location. We find this coincidence to be strong support for the interpretation of the non-thermal broadening as being due to turbulence, rather than waves or bulk flows along the line of sight. Similar to the EIS non-thermal speeds, the LCT speeds were also inspected in four smaller boxes as indicated in Figure 13: the median plane-of-sky speeds in these boxes range from 13 km s<sup>-1</sup> to 67 km s<sup>-1</sup>, increasing with height as shown in Table 8. This increase of speed with height is also consistent with the increase seen in the EIS non-thermal speeds, an observational finding for which we know of no precedent. However, we note that the AIA and EIS boxes do not have significant overlap except for box 1 and 1H. There is a much better overlap between the AIA boxes in Figure 13 and the EIS boxes to be described later in Figure 16.

### 3.5. Sources of Error

The instrumental widths of the EIS spectral lines are a substantial fraction of their total widths due to the difficulty of constructing a high spectral resolution EUV spectrometer. Thus, care must be exercised in interpreting line width. The main errors involved in determining the non-thermal motions are (1) statistical errors in total observed line width; (2) uncertainties in the instrumental width; (3) uncertainties in the thermal Doppler width due to uncertainties in the ionization balance, line excitation atomic physics, and the differential emission measure; and (4) errors introduced due to warm pixels. Determining the sum of these errors is difficult.

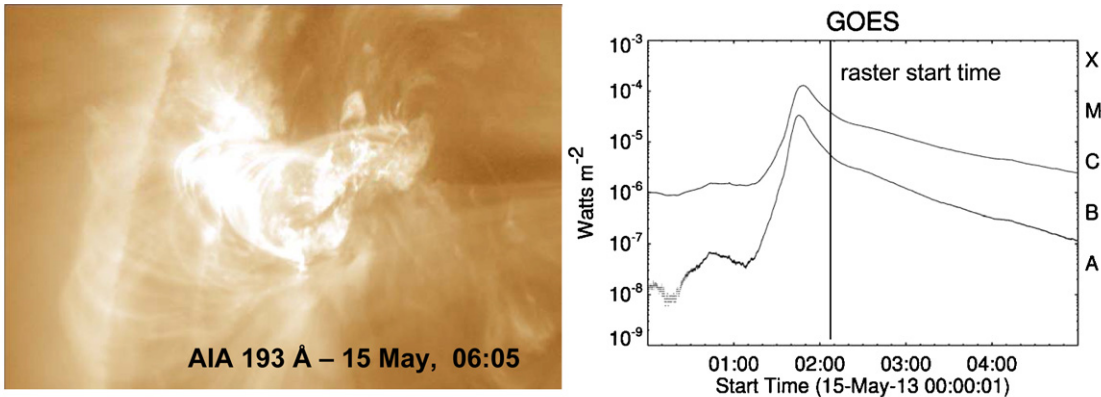


**Figure 9.** Top left: an AIA 193 Å image for the 2013 May 15 flare; top right: GOES data for the May 15 flare; bottom: EIS intensity images (log scale) for the indicated lines.

(A color version of this figure is available in the online journal.)

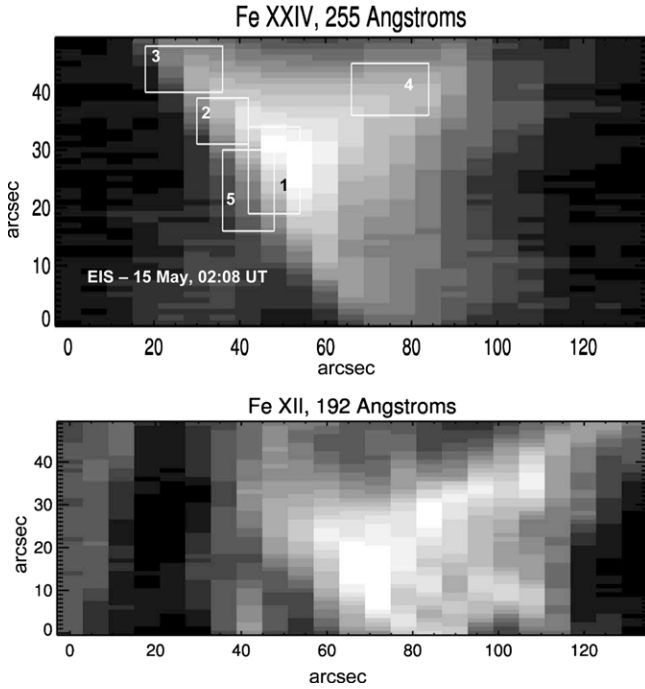


**Figure 10.** Intensity images in Fe xxiv and a line of Fe xii at 192.39 Å for the 2013 May 15 flare. The boxes indicate areas in which average non-thermal motions and temperatures were computed (see Table 7).

Two methods were used to calculate average non-thermal motions in boxes. In one method, the non-thermal speeds obtained from Gaussian fits to every pixel in a box are averaged over the box. However, non-thermal speeds less than zero (bad data) are excluded, and pixels with temperatures less than 4 MK and greater than 20 MK are also excluded as being unreasonable

for temperatures determined from the Fe xxiii/Fe xxiv line ratio. The number of pixels that were not excluded was also calculated along with the total number of pixels in a box. Boxes with most pixels excluded indicate a box where the data are not very good and therefore non-thermal motions in such a box are not reliable.

In a second method, a profile for the entire box is built up by summing the intensity of each pixel at each wavelength covered by the line profile for every pixel in the box. The restriction here is that intensity and intensity statistical error must be a positive quantity in order to be included in the sum. The squares of the statistical errors are also summed. The resulting summed profile over the box is fit by a Gaussian with statistical measured errors for every position in the profile equal to the square root of the summed squares of the individual errors. There is no restriction on the temperature that is summed over the entire box to produce an average thermal temperature. Similarly, the instrumental width is averaged over the box. Removal of the instrumental and thermal widths from the summed profile yields an average non-thermal speed for the box.

The non-thermal speeds obtained by each method are compared. If there are large differences ( $\approx 30\%-40\%$ ), the data are considered unreliable. The summed profiles obtained by the second method are plotted along with the errors and the Gaussian fits. These profiles are inspected by eye. If the profiles are noisy due to poor statistics or the Gaussian routine simply does not fit them, the data are rejected. It is hoped that these procedures weed out most of the bad data and give reliable results.

The statistical errors are generally small. In the case of a weak line the errors are about 10% in the line width, giving a  $1\sigma$  error of about  $5 \text{ km s}^{-1}$ . The total errors are larger because of errors in temperature and some bad data that elude being discarded.

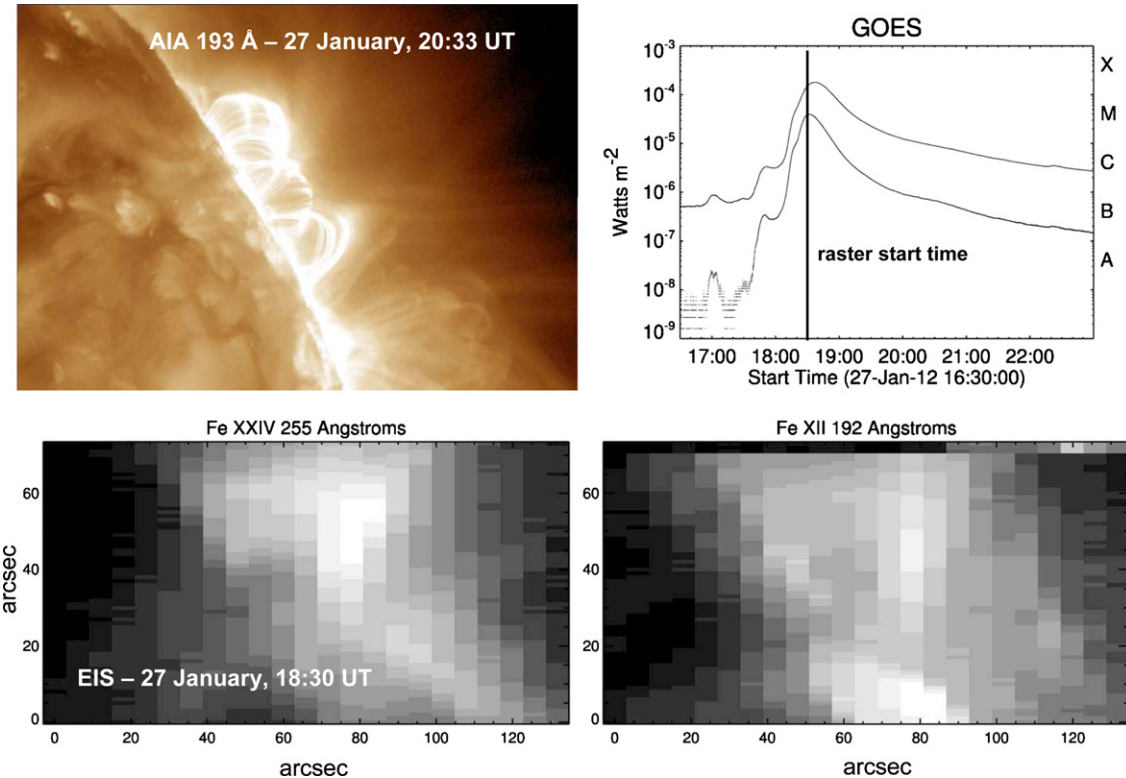


**Figure 11.** Top left: an AIA 193 Å image for the 2012 January 27 flare; top right: GOES data for the January 27 flare; bottom: EIS intensity images (log scale) for the indicated lines.

(A color version of this figure is available in the online journal.)

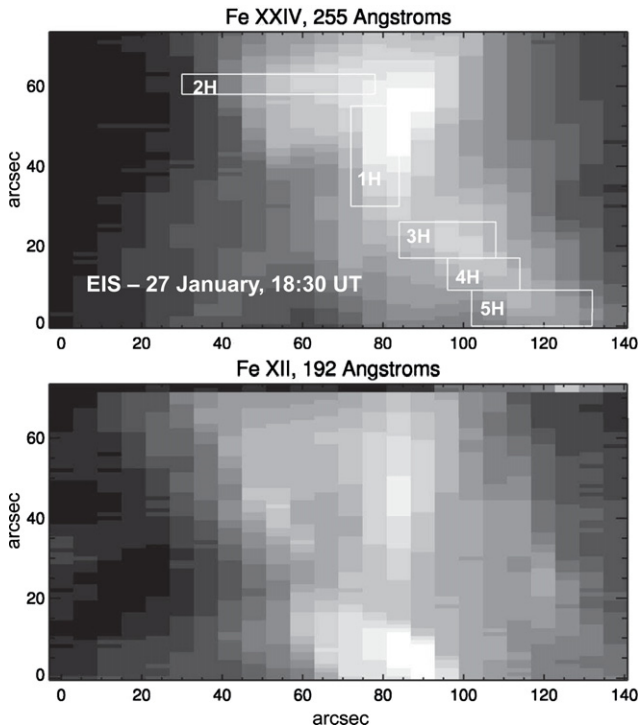


**Figure 12.** Intensity images in Fe xxiv and a line of Fe xii at 192.39 Å for the 2012 January 27 flare. The boxes indicate areas in which average non-thermal motions and temperatures were computed (see Table 8).

Scattered light can influence the line profiles. There is the scattered light that appears everywhere, and there are the diffraction spikes that produce diffraction images when the intensity of a feature is very large, as in a flare near flare

maximum. For our events, the diffraction pattern is not visible for three of the events. For the June 7 event there is a quite weak pattern, but an investigation of the Fe xxiv profiles in and out of this pattern does not show an obvious effect on the line profile, so we conclude that diffraction patterns are not an issue for this work. This is because our observations are mostly beyond peak EUV flux.

Hahn et al. (2012) have carefully examined the pervasive scattered light in a study of EIS spectra above the solar limb in their work on wave heating. The pervasive scattered light would tend to narrow our line profiles as the intensity of the real component decreases. This is because the scattered light arises from intense regions at the flare loop tops where the profile is narrow after the impulsive phase ceases. This is in the opposite direction of our results. Furthermore, Hahn et al. (2012) found that a huge contribution of scattered light (greater than 45%) was necessary to begin influencing their results. Because of the Hahn et al. (2012) results and the fact that scattered light produces an effect opposite to the effect we are claiming to have found, we feel that scattered light is unimportant for this work.

Errors in temperature are difficult to determine because they arise from a number of possible sources. We note that the temperatures are consistent with *Yohkoh* flare temperatures and measurements done using the same lines for a *Skylab* flare (Doschek & Feldman 1996). But perhaps most convincing is that a differential emission measure analysis of the same type of structure, i.e., the reconnection region, in another flare yielded temperatures near 13 MK (Savage et al. 2012; McKenzie 2013).

The most compelling reason for accepting the non-thermal results in this paper is the overall consistency of the data for the Fe xxiii and Fe xxiv lines. Random results due to overwhelming errors would not produce any consistency. This consistency is

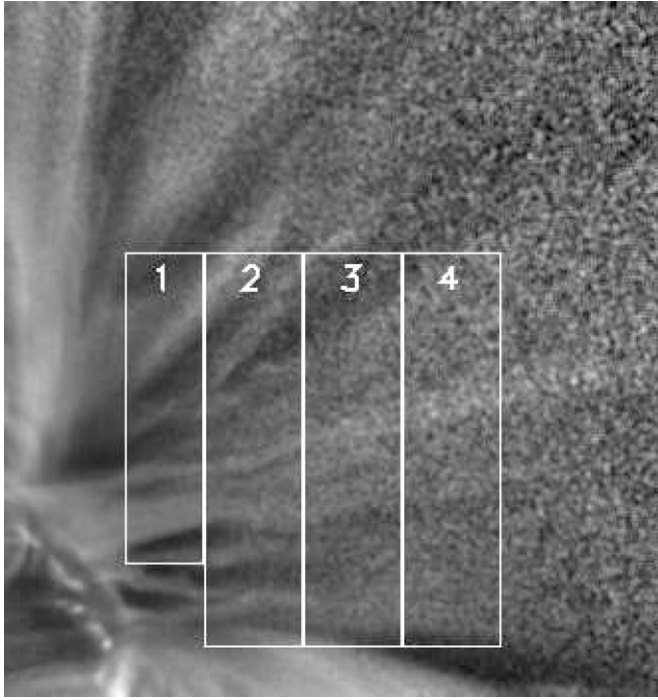


**Figure 13.** 131 Å AIA filter image of the 2012 January 27 flare. Non-thermal motions are derived using an LCT technique. The speeds for the four boxes 1, 2, 3, and 4 are 13, 23, 47, and 67 km s<sup>-1</sup>, respectively.

quite apparent in the last set of boxes calculated and discussed in the next section.

#### 4. DISCUSSION

There are five general results obtained in the previous section: (1) the highest temperatures occur in the largest structures, (2) the non-thermal motions in the multimillion-degree regions increase with height above the bright coronal flare loops, (3) the non-thermal multimillion-degree motions are 40–60 km s<sup>-1</sup>, (4) the non-thermal motions for coronal temperatures along the same path lengths as the multimillion-degree plasma remain constant around 20–30 km s<sup>-1</sup>, and (5) the multimillion-degree temperature is about 11–15 MK.

We can emphasize the dependence of non-thermal motions with height above the loop tops by plotting paths on the images and averaging the non-thermal motions over these paths. For the May 17 event, the path is basically the *X* axis, and the figures discussed earlier give results as a function of height as well as position along the loop arcade. However, the paths for the other three flares are not so simple, so we show path results for these events.

In Figure 14, we show the approximate plane-of-the-sky path for the June 7 event, as determined from *SDO* images via JHelioviewer. Although the *SDO* images are saturated around the times of the EIS raster, the later images show the 1 MK post-flare loops and the arcade orientation. The bottom part of Figure 14 shows the non-thermal motions averaged over the boxes. The reader can estimate heights above the loop arcades projected against the plane of the sky. The multimillion-degree lines show a clear increase in non-thermal motions and agree pretty well with each other. The cooler line behavior does not exhibit an increase. The two cooler lines come from the flare and background coronal emission, so their behavior is hard to predict.

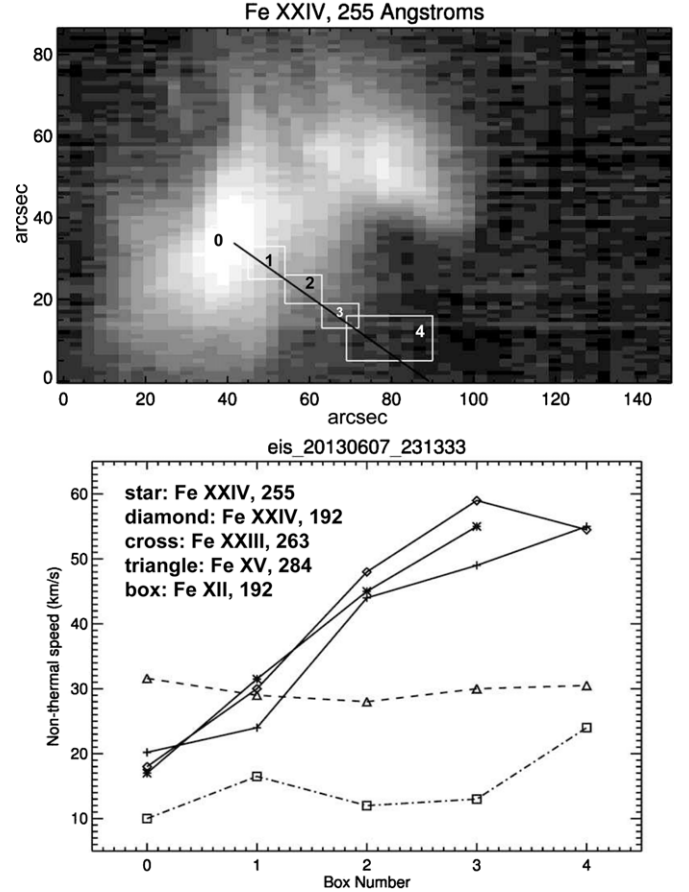


**Figure 14.** Top: image of the June 7 flare in Fe xxiv. The solid black line is the rough direction above the loop arcade. Bottom: non-thermal speeds in the indicated lines averaged over the indicated box.

In Figure 15, we show a similar pattern for the May 15 event. In the case of the May 15 flare the *SDO* images indicated that the EIS line of sight would intercept the loop tops unless quite far above them. The *SDO* data indicate that the hottest regions are at the far eastern end of the path shown in the figure. So this event is a bit complicated because at some positions the EIS line of sight must intercept the loop tops. However, the bottom panel of the figure shows that the weaker far eastern emission has larger non-thermal motions. The line of sight for this region does not intercept bright loop tops.

Figure 16 shows results for the January 27 flare, which look quite similar to the other flare results. In order to lessen saturation problems, we show results obtained from a slightly later raster than the raster results shown in Table 7. In this case the Fe xv line also shows an increase with height, but because the lower temperature lines are composed of flare and background emission, variable results can be expected.

Because the three high-temperature lines of Fe xxiii and Fe xxiv show similar quantitative behavior with height and position in the flare images, we are confident in the overall non-thermal speed conclusions considering the sources of error discussed in Section 3.5 and our procedures in deriving non-thermal speeds. The similar trend of height-dependent turbulent speeds observed with AIA reinforces this conclusion.

Our results appear to be consistent with much current thinking regarding the standard model. In current thinking, the plasma heating occurs in outflows and downflows outside of the actual flare reconnection region. Some evidence for this is the

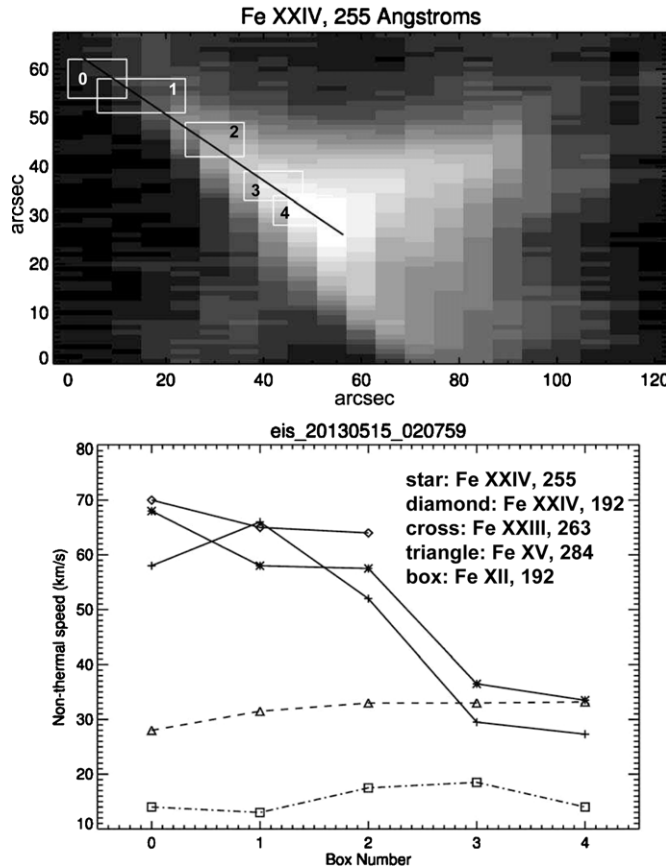


**Figure 15.** Top: image of the May 15 flare in Fe xxiv. The solid black line is the rough direction above the loop arcade. Bottom: non-thermal speeds in the indicated lines averaged over the indicated box.

discovery, from hard X-ray images and spectra obtained from *RHESSI*, of a double loop top hard X-ray source, indicating bi-directional flows out of the reconnection region (e.g., Sui & Holman 2003; Liu et al. 2008; Caspi & Lin 2010). Very recently, Liu et al. (2013) have given dramatic evidence for plasma heating outside the reconnection region with a schematic of the processes shown in Figure 12 of their paper. Our observations concern the downflows toward the bright reconnected post-flare loops depicted in their schematic.

Liu et al. (2008) interpret their results in terms of a model developed by Hamilton & Petrosian (1992), who suggest that thermal electrons can be stochastically accelerated to non-thermal energies by electron whistler wave interactions in a turbulent plasma (see Figure 1 in Liu et al. 2008). We suggest that this turbulence might produce the spectral line broadening that we observe. Purely theoretically, Linton & Longcope (2006) and Longcope et al. (2010) have calculated reconnection using a three-dimensional MHD model. A pair of reconnected flux tubes is produced by the reconnection, creating supersonic inflows that produce shocks. The shocks compress and heat plasma, thus driving the energetics of the standard flare model. Hot multimillion-degree flare plasma is produced in the vicinity of the reconnection region. Linton & Longcope (2006) propose that the downward-moving voids mentioned above that were first seen in *Yohkoh* soft X-ray images and discussed by McKenzie & Hudson (1999) and McKenzie (2000) are produced by this post-reconnection process.

Our contribution to the observations near the reconnection region is the measurement of apparent turbulence in EIS and

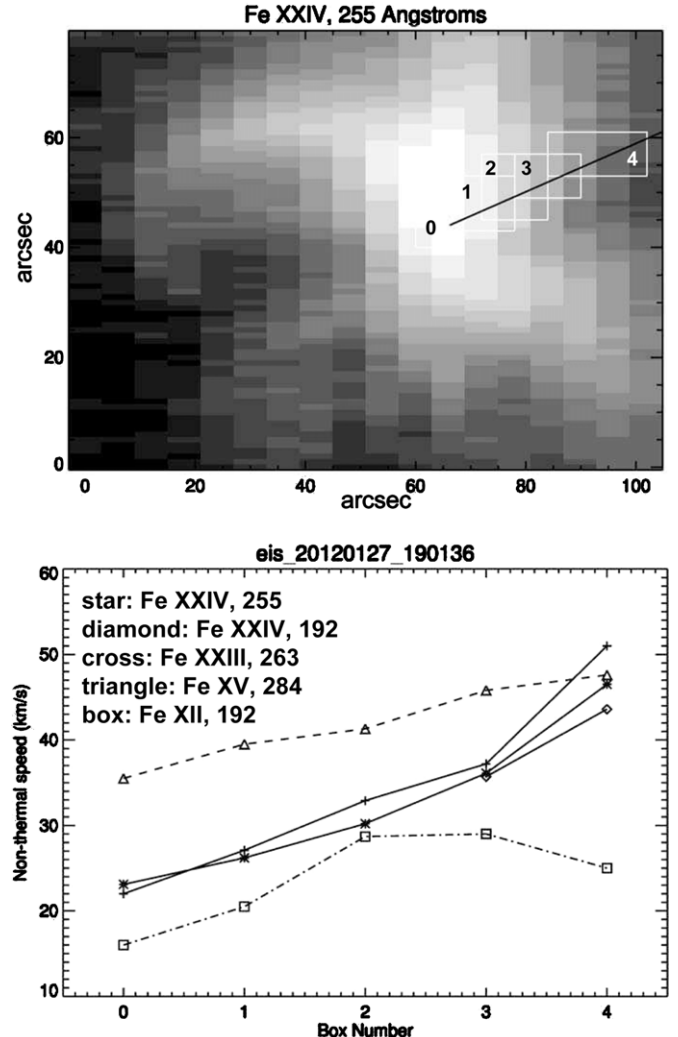


**Figure 16.** Top: image of the January 27 flare in Fe xxiv. The solid black line is the rough direction above the loop arcade. Bottom: non-thermal speeds in the indicated lines averaged over the indicated box.

AIA images that is consistent with plasma heating outside the reconnection region. The possibility of turbulent reconnection as a consequence of magnetic reconnection has also been suggested by Susino et al. (2013) for outward-moving plasma heating between the reconnection region and a CME. We might expect this turbulence (and electron temperature) to vary with height above the closed post-flare loops. The largest turbulence and temperature would be produced in the newest formed loops, which would be the largest loops closest to the reconnection region. As the loops cool, the turbulent energy and temperature would decrease toward the already closed post-flare loops. In summary, the results to take away from this paper are those summarized in the tables and, e.g., in Figures 2, 14, 15, and 16. We have presented the behavior of non-thermal line broadening and temperature as a function of height above the closed post-flare loops, as measured by a high-resolution EUV imaging spectrometer.

Since we are interested in flare energy release and the proximity to the reconnection region, it is useful to ask what happens above the multimillion-degree loops that we see. Does the temperature increase? Do the non-thermal motions continue to increase? We can infer answers to these questions

by reviewing results from high-resolution Bragg crystal X-ray spectra obtained in the 1980s.

Finally, we conclude this paper by attempting to relate our current observations to observations made previously in the 1980s by three no longer operating missions: the DoD Space Test Program mission *P78-1*, the NASA *SMM*, and the Japanese *Hinotori* mission. All three of these missions contained high-resolution BCS that operated between about 1.5 and 25 Å.

The X-ray spectra from *P78-1*, *SMM*, and the *Hinotori* mission had sufficient spectral resolution to measure accurate line profiles for the resonance lines of H-like and He-like ions found at wavelengths less than about 25 Å. Accurate average electron temperatures were available from dielectronic to resonance line ratios, and the instrumental widths were small compared with the physical line widths. Although there was a complication with source size, reliable non-thermal motions could be obtained from Gaussian fits to resonance line profiles. Unfortunately, spatial resolution was virtually non-existent. A discussion of the X-ray spectra with results is given by Doschek (1990).

The highest temperature lines available for solar flares are the H-like and He-like lines of iron and their associated satellite lines between about 1.75 and 2 Å. They are strong in flares, and studies were made of flare temperature as a function of *GOES* flare class (e.g., Feldman et al. 1995). The result was that the highest temperature in most flares for the thermal plasma (not the superhot component visible in some flares) is about 25 MK (e.g., Feldman et al. 1995). However, the peak of the He-like iron contribution function is about 52 MK, so to get a temperature significantly less than this implies a decreasing emission measure with temperature (e.g., Doschek & Feldman 1987). Nevertheless, temperatures obtained from He-like iron (Fe xxv) lines and satellites were always higher than temperatures obtained from SXT on *Yohkoh*, from lower temperature X-ray lines such as the resonance line of Ca xix, or from the Fe xxiv lines in the EUV as observed by EIS.

We must conclude that the regions of the flare that emit Fe xxv are not detectable by EUV instrumentation. No strong lines exist in the EUV to measure the high temperatures observed by the Bragg spectrometers. There are very weak EUV lines of, e.g., Fe xxv, but they have not yet been seen in EIS spectra. However, because high temperatures appear to occur hierarchically with height in flares, it is interesting to compare the non-thermal motions obtained from the X-ray spectra with the values obtained by EIS at lower altitudes. We assume that the high-temperature X-ray lines seen in X-ray spectra arise from plasma at the tops of loops that are formed at higher altitudes than the Fe xxiv loops seen in the EUV.

The non-thermal motions obtained from profiles of the He-like Fe xxv resonance line at 1.85 Å and other resonance lines such as the Ca xix line are quite large, more than 100 km s<sup>-1</sup>, and these motions decrease during the flare rise phase to about 20–60 km s<sup>-1</sup> at peak and beyond. It was difficult to measure non-thermal motions beyond the flare peak due to thermal and other line broadening. The increase of non-thermal speed with height in the EIS spectra is expected based on the large non-thermal speeds inferred from previously obtained X-ray line profiles.

*Hinode* is a Japanese mission developed and launched by ISAS/JAXA, collaborating with NAOJ as a domestic partner, and NASA (USA) and STFC (UK) as international partners. Scientific operation of the *Hinode* mission is conducted by

the *Hinode* science team organized at ISAS/JAXA. This team mainly consists of scientists from institutes in the partner countries. Support for the post-launch operation is provided by JAXA and NAOJ, STFC, NASA, ESA (European Space Agency), and NSC (Norwegian Space Center). We are grateful to the *Hinode* team for all their efforts in the design, build, and operation of the mission. G.A.D. and H.P.W. acknowledge support from the NASA *Hinode* program and from ONR/NRL 6.1 basic research funds. D.M.’s contribution was supported by NASA under contract SP02H3901R from Lockheed-Martin to Montana State University and contract NNM07AB07C with the Smithsonian Astrophysical Observatory.

## REFERENCES

- Antonucci, E., Rosner, R., & Tsinganos, K. 1986, *ApJ*, **301**, 975  
 Caspi, A., & Lin, R. P. 2010, *ApJL*, **725**, L161  
 Culhane, J. L., Harra, L. K., James, A. M., et al. 2007, *SoPh*, **243**, 19  
 Czakowska, A., de Pontieu, B., Alexander, D., & Rank, G. 1999, *ApJL*, **521**, L75  
 Doschek, G. A. 1990, *ApJS*, **73**, 117  
 Doschek, G. A., Antiochos, S. K., Antonucci, E., et al. 1986, in *Energetic Phenomena on the Sun*, ed. M. R. Kundu & B. E. Woodgate (NASA Conference Publication, Vol. 2439; Hampton, VA: NASA STI), 1  
 Doschek, G. A., & Feldman, U. 1987, *ApJ*, **313**, 883  
 Doschek, G. A., & Feldman, U. 1996, *ApJ*, **459**, 773  
 Doschek, G. A., Warren, H. P., & Young, P. R. 2013, *ApJ*, **767**, 55  
 Drake, J. F., Swisdak, M., Che, H., & Shay, M. A. 2006, *Natur*, **443**, 553  
 Feldman, U., Doschek, G. A., Behring, W. E., & Phillips, K. J. H. 1996, *ApJ*, **460**, 1034  
 Feldman, U., Doschek, G. A., Mariska, J. T., & Brown, C. M. 1995, *ApJ*, **450**, 441  
 Golub, L., Deluca, E., Austin, G., et al. 2007, *SoPh*, **243**, 63  
 Hahn, M., Landi, E., & Savin, D. W. 2012, *ApJ*, **753**, 36  
 Hamilton, R. J., & Petrosian, V. 1992, *ApJ*, **398**, 350  
 Hara, H., Watanabe, T., Harra, L. K., Culhane, J. L., & Young, P. R. 2011, *ApJ*, **741**, 107  
 Hara, H., Watanabe, T., Matsuzaki, K., et al. 2008, *PASJ*, **60**, 275  
 Harra, L. K., Williams, D. R., Wallace, A. J., et al. 2009, *ApJL*, **691**, L99  
 Imada, S., Aoki, K., Hara, H., et al. 2013, *ApJL*, **776**, L11  
 Innes, D. E., McKenzie, D. E., & Wang, T. 2003, *SoPh*, **217**, 247  
 Kosugi, T., Matsuzaki, K., Sakao, T., et al. 2007, *SoPh*, **243**, 3  
 Landi, E., Young, P. R., Dere, K. P., Del Zanna, G., & Mason, H. E. 2013, *ApJ*, **763**, 86  
 Lemen, J. R., Title, A. M., Akin, D. J., et al. 2012, *SoPh*, **275**, 17  
 Linton, M. G., & Longcope, D. W. 2006, *ApJ*, **642**, 1177  
 Liu, W., Chen, Q., & Petrosian, V. 2013, *ApJ*, **767**, 168  
 Liu, W., Petrosian, V., Dennis, B. R., & Jiang, Y. W. 2008, *ApJ*, **676**, 704  
 Longcope, D. W., Des Jardins, A. C., Carranza-Fulmer, T., & Qiu, J. 2010, *SoPh*, **267**, 107  
 Mariska, J. T., & Doschek, G. A. 1997, *ApJ*, **485**, 904  
 Mariska, J. T., & McTiernan, J. M. 1999, *ApJ*, **514**, 484  
 McKenzie, D. E. 2000, *SoPh*, **195**, 381  
 McKenzie, D. E. 2013, *ApJ*, **766**, 39  
 McKenzie, D. E., & Hudson, H. S. 1999, *ApJL*, **519**, L93  
 McKenzie, D. E., & Savage, S. L. 2009, *ApJ*, **697**, 1569  
 Milligan, R. O. 2011, *ApJ*, **740**, 70  
 Milligan, R. O., & Dennis, B. R. 2009, *ApJ*, **699**, 968  
 O’Dwyer, B., Del Zanna, G., Mason, H. E., Weber, M. A., & Tripathi, D. 2010, *A&A*, **521**, A21  
 Reeves, K. K., Warren, H. P., & Forbes, T. G. 2007, *ApJ*, **668**, 1210  
 Savage, S. L., McKenzie, D. E., & Reeves, K. K. 2012, *ApJL*, **747**, L40  
 Sheeley, N. R., Jr., Warren, H. P., & Wang, Y.-M. 2004, *ApJ*, **616**, 1224  
 Sui, L., & Holman, G. D. 2003, *ApJL*, **596**, L251  
 Susino, R., Bemporad, A., & Krucker, S. 2013, *ApJ*, **777**, 93  
 Tsuneta, S. 1996, *ApJ*, **456**, 840  
 Wang, T., Sui, L., & Qiu, J. 2007, *ApJL*, **661**, L207  
 Warren, H. P., & Doschek, G. A. 2005, *ApJL*, **618**, L157  
 Warren, H. P., Mariska, J. T., & Doschek, G. A. 2013, *ApJ*, **770**, 116  
 Warren, H. P., O’Brien, C. M., & Sheeley, N. R., Jr. 2011, *ApJ*, **742**, 92  
 Yamada, M., Kulsrud, R., & Ji, H. 2010, *RvMP*, **82**, 603  
 Yokoyama, T., Akita, K., Morimoto, T., Inoue, K., & Newmark, J. 2001, *ApJL*, **546**, L69  
 Young, P. R., Doschek, G. A., Warren, H. P., & Hara, H. 2013, *ApJ*, **766**, 127  
 Zweibel, E. G., & Yamada, M. 2009, *ARA&A*, **47**, 291